Biophysical Journal Volume 68 May 1995 1776–1786

Low Resolution Structure of Bovine Rhodopsin Determined by Electron Cryo-Microscopy

Vinzenz M. Unger and Gebhard F. X. Schertler
Laboratory of Molecular Biology, Cambridge CB2 2QH, United Kingdom

ABSTRACT The visual pigment rhodopsin is a member of the G protein-coupled receptor family. Electron cryo-microscopy was used to determine the three-dimensional structure of bovine rhodopsin from tilted two-dimensional crystals embedded in vitrified water. The effective resolution in a map obtained from the 23 best crystals was about 9.5 Å horizontally and approximately 47 Å normal to the plane of the membrane. Four clearly resolved tracks of density in the map correspond to four α-helices oriented nearly perpendicular to the plane of the membrane. One of these helices appears to be more tilted than anticipated from the projection structure published previously. The remaining three helices are presumably more highly tilted, given that they form a continuous "arc-shaped" feature and could not be resolved to the same extent. The overall density distribution in the low resolution map shows an arrangement of the helices in which the "arc-shaped" feature is extended by a fourth, less tilted helix. The band of these four tilted helices is flanked by a straight helix on the outer side and a pair of straight helices on its inner side.

INTRODUCTION

In the vertebrate retina, the light receptor rhodopsin is found in the outer segments of the rod cells. Light sensitivity is conferred by the chromophore 11-*cis*-retinal, which is covalently attached to the ϵ-amino group of Lys296 in the seventh transmembrane domain. In the ground state the protonated Schiff base is stabilized by the counterion Glu113 in the third transmembrane domain (Sakmar et al., 1989, Zhukovsky and Oprian, 1989). The light-induced isomerization of the retinal to the all-*trans* conformation triggers a G protein-coupled signal transduction cascade, leading to the closure of cGMP-dependent cation channels in the plasma membrane of the rod outer segment (Fresenko et al., 1985). The resulting hyperpolarization of the membrane eventually lowers the rate of transmitter release in the synaptic part of the photoreceptor, triggering responses in bipolar cells.

Protein sequence data (Hargrave et al., 1983; Ovchinnikov et al., 1982), circular dichroism spectroscopy (Chabre, 1978; Shichi and Shelton, 1974), Fourier transform infrared spectroscopy (Lamba et al., 1994), infrared linear dichroism (Michel-Villaz et al., 1979) and neutron scattering experiments (Saibil et al., 1976) suggest that about 50% of the 348 rhodopsin residues are in an α-helical conformation. The projection structure of bovine rhodopsin at 9 Å resolution, obtained by electron cryo-microscopy for the first time provided experimental evidence that the polypeptide within the membrane interior contains α-helices (Schertler et al., 1993). In addition, the projected structure of rhodopsin indicated that the arrangement of the putative transmembrane helices is different from that determined for bacteriorhodopsin, the light-driven proton pump found in *Halobacteria* (Baldwin et al., 1988; Unwin and Henderson, 1975). This suggested that the detailed three-dimensional (3D) structures of bovine rhodopsin, and hence the structure of G protein-coupled receptors in general, may be different from that of bacteriorhodopsin despite their similar overall membrane topology.

Results obtained for bacteriorhodopsin (Henderson et al., 1990) and the light-harvesting complex LHCII from green plants (Kühlbrandt et al., 1994) show that high resolution electron cryo-microscopy is an alternative to x-ray crystallography for the determination of protein structures at atomic resolution. This applies especially to integral membrane proteins, where well-ordered 3D crystals are not easily obtained. Furthermore, recent studies on the nicotinic acetylcholine receptor (Unwin, 1993, 1995) and the sarcoplasmic Ca^{2+}-ATPase (Toyoshima et al., 1993) demonstrate that useful 3D structural information about membrane proteins can be derived from lower resolution maps. This emphasizes the versatility of electron cryo-microscopy to gain insight into the structure of membrane proteins at different levels of resolution.

To investigate further the structure of bovine rhodopsin, images of tilted two-dimensional (2D) crystals embedded in vitrified water were recorded. Image analysis was subsequently used to obtain the first 3D map of a G protein-coupled receptor, showing details beyond 10 Å resolution within the plane of the membrane.

MATERIALS AND METHODS

n-Octyltetraoxyethylene (C_8E_4) and soybean phosphatidylcholine were obtained from Bachem (Bubendorf, Switzerland) and Sigma Chemical Co. (St. Louis, MO) respectively. Copper-rhodium electron microscope grids were purchased from Graticules, Ltd. (Tonbridge, UK).

Rhodopsin isolation and 2D crystallization

Rhodopsin was isolated from bovine rod outer segments as described previously (DeGrip, 1982; Schertler et al., 1993). Purified rhodopsin was re-

Received for publication 4 August 1994 and in final form 10 February 1995.

Address reprint requests to Dr. Vinzenz M. Unger, Laboratory of Molecular Biology, MRC, Hills Road, Cambridge CB2 2QH, UK. Tel.: 44-1223-402291; Fax: 44-1223-213556.

0006-3495/95/05/1776/11 $2.00

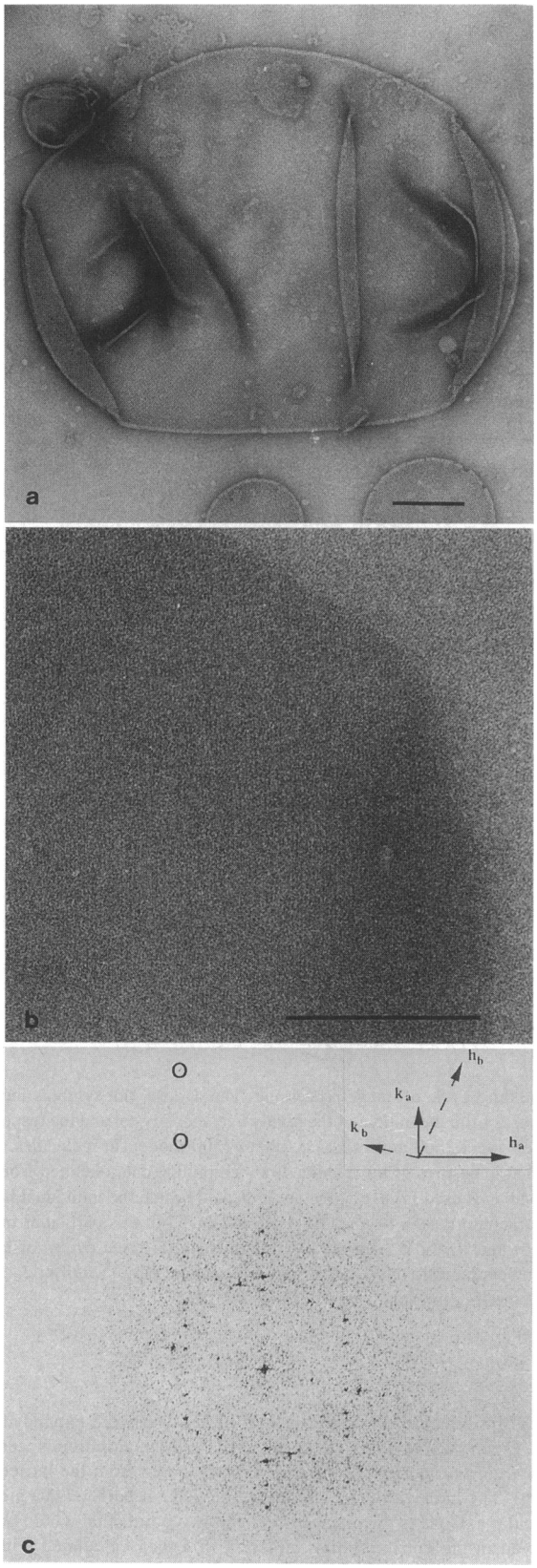

FIGURE 1 (*a*) Phosphatidylcholine vesicle stained with 1% uranyl acetate for 10 s. A 2D rhodopsin crystal can be detected along the lower straight edge of the vesicle. The scale bar represents 0.2 μm. (*b*) Magnified view of a rhodopsin crystal preserved in vitrified water. The appearance of the vesicle compared with the amorphous carbon film in the upper right corner emphasizes the greatly reduced contrast of low dose cryo-images. The scale bar represents 0.2 μm. (*c*) Calculated Fourier transform of the best tilted crystal before image processing. The diffraction spots arising from two independent layers can easily be seen. A schematic representation of the main lattice vectors of both crystals is shown in the insert. For the better of the two lattices the (−1,10) and (−1,13) reflections can be seen (circled spots), with the latter spot corresponding to about 10.8 Å resolution. For convenience the Friedel mates of these two reflections were omitted from the figure.

constituted in soybean phosphatidylcholine. Reconstitutions were set up in dim red light using 3–30 lipids per rhodopsin molecule at a rhodopsin concentration of 1 mg/ml in 20 mM HEPES pH 7.0, 0.1 M NaCl, 10 mM $MgCl_2$, 1 mM dithiothreitol, and 3 mM NaN_3 at 20°C. The detergent (0.2% C_8E_4) was removed by dialysis and a small number of 2D crystals with dimensions up to 0.5 μm × 0.5 μm formed after 5–20 days, but only from freshly prepared rhodopsin. The results of these crystallizations were not very reproducible probably because of changes in the starting material, which was derived from different rhodopsin preparations. Samples were kept at 4°C in the dark and remained unchanged over a period of several months. Upon exposure to white light, the vesicle suspension first appeared red and then turned yellow. This behavior indicates that the reconstituted material is likely to be fully functional rhodopsin.

Specimen preparation

Carbon-coated electron microscope grids were prepared according to standard procedures (Henderson et al., 1990) and glow discharged in the presence of amyl amine directly before use. All manipulations of the sample before negative staining with 1% (w/v) uranyl acetate or cryo-preservation were carried out in dim red light to avoid bleaching of the chromophore. For the preparation of frozen grids, pretreatment of the grids with a 0.05% (v/v) *n*-octyltetraoxyethylene (C_8E_4) solution for about 30 s facilitated spreading of the specimen and enhanced the formation of thinner and more even layers of vitrified water.

Recording and processing of electron micrographs

Electron micrographs were recorded on Kodak SO-163 film using either a Philips CM12 or Philips 420 (Cambridge, U.K.) electron microscope at 120 kV with 50-μm condenser and objective apertures. A GATAN (Gatan Ltd., Corby, U.K.) cold stage was used for the work with frozen grids, and micrographs were recorded under standard low dose conditions at −170°C, nominal tilt angles of up to 30°, and a magnification of 35,000. Films were developed in full-strength D19 developer for 5 min at 20°C. The average electron dose received by the specimen was about 11 el/Å^2 as determined from the optical densities of the films.

Films were screened by optical diffraction to identify crystalline arrays of rhodopsin. Areas of 2 cm × 2 cm from images of the best crystals were digitized on a Joyce-Loebl densitometer (10-μm steps corresponding to a spacing of 2.9 Å at the level of the specimen) and processed using a standard protocol (Henderson et al., 1986, 1990). Each processing step was adapted to optimize it for the very small crystals found in the rhodopsin specimen. Boxing off the precise area of crystallinity was essential to minimize the background noise to a level that allowed the higher resolution Fourier components to be obtained at the end of three cycles of lattice unbending.

The final set of phases for each film was corrected for the effects of the contrast transfer function (CTF). An initial estimate of the amount of defocus was obtained by determining the position of the first zero of the CTF in the optical diffraction pattern. After the determination of the common phase origins, data from the 23 best crystalline areas were combined. This data set was used for further refinement of the defocus values as well as the astigmatism. These corrections were done by finding the defocus for which the best phase residual was obtained in the determination of the phase origin for a particular image against the whole data set. After two cycles of defocus

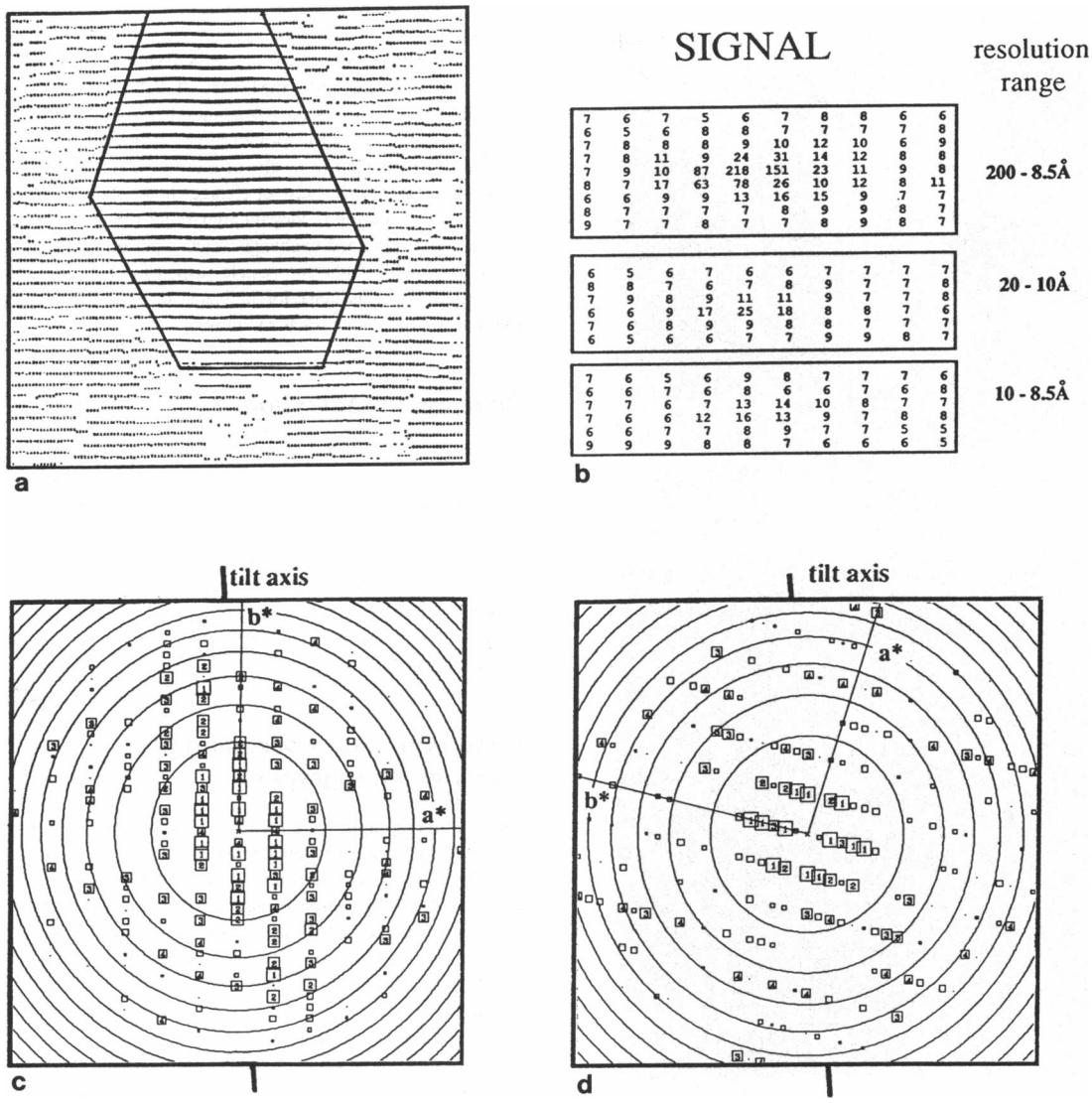

FIGURE 2 (*a*) Real space cross-correlation map for lattice RE081A obtained in the third cycle of image processing. The darkest plot symbols indicate ≥70% similarity for the correlation peak, calculated from a 150 × 150-pixel reference area from the middle of the highly averaged crystal and the respective unit cells within the crystal lattice. The largest continuous part of the crystal contained about 1800 unit cells, i.e., about 7200 rhodopsin molecules. Only this part was finally used to extract the amplitudes and phases (boxed area). (*b*) Scaled intensities of the averaged raw amplitude data obtained from the boxed area in Fig. 2 *a* at the end of the third cycle of image refinement. The resolution bands used for averaging are indicated beside the individual boxes. A significant peak is still present between 8.5 and 10 Å resolution, indicating that structural details beyond 10 Å are preserved in this particular image. (*c* and *d*) Calculated diffraction patterns for lattices RE081A (defocus 9530, 9150,0) and RE081B (defocus 8630, 8250,0) after three cycles of lattice straightening. Both crystals were tilted by 13° with regard to the marked tilt axis. Numbers indicate the signal-to-rms background ratio (1, ≥8×; 2, ≥4×; 3, ≥2.6×; 4, ≥2×; grades 5, 6, 7, and 8 are encoded by decreasing box sizes). The circles represent zero values in the CTF.

and astigmatism refinement and remerging of the data, lattice lines were fitted by hand to the experimental phase data. The amplitudes were scaled to correct for the CTF, and curves were fitted using the program LATLINE (Agard, 1983).

Projection and 3D maps were calculated by using the crystallographic CCP4 program suite. Amplitude correction was performed by applying temperature factors up to −1000 Å^2 to sharpen the data. For the calculation of 3D maps, Fourier components were sampled at 0.005 Å^{-1} (implying a unit cell along the *c* axis of 200 Å), and maps were printed in sections separated by 5 Å.

The effective resolution of the final data set was estimated from its point spread function, i.e., the Fourier transform of the distribution of the data sample points, with each point weighted according to its accuracy. In this case, the experimental p222$_1$ data were expanded into space group p1, the phases were set to 0°, and the amplitudes were set to the figure of merit values (range 0–1, obtained from the lattice line fitting). The half-width (i.e., width of the peak at half-height) along a particular axis gives the distance between two points that would be just resolved in the corresponding direction in a map calculated with the data. Because the resolution of electron density maps is more usually given in terms of the Fourier cutoff rather than the half-width of the point spread function, the half-widths along the three axes were converted to effective Fourier cutoff resolutions. The conversion factor needed to do this was obtained by calculating the half-widths for an ideal data set that included all terms up to a 9.0 Å cutoff and a maximum tilt angle of 20° (see Fig. 3 *c*).

TABLE 1 Summary of data

Film	TAXA	TANGL	Defocus	Spots (IQ 1–5)	ΔΦ	Spots (IQ 1–8)	ΔΦ
23312	0.0	0.9	11900, 11800, −70	73	28.8	107	40.8
23331	80.0	0.9	11800, 1800, −20	71	31.8	103	42.0
23313	50.0	0.9	11635, 11635, 45	63	40.0	118	51.8
23314	70.0	0.9	11800, 11800, −20	52	50.2	95	67.1
20451	−65.0	−3.0	9480, 8400, 45	50	30.0	108	45.3
1778	−32.0	3.0	7900, 8500, 20	60	39.1	112	52.2
17781	−68.0	3.0	8100, 8700, 20	53	42.5	106	56.1
783	80.0	−4.0	5500, 5500, 45	48	34.8	97	56.3
012	130.0	−7.0	11000, 10750, 0	61	33.4	109	46.5
95722	75.0	−7.0	5500, 5500, 0	66	48.4	103	54.6
011	35.0	7.0	11000, 11000, 45	49	29.9	94	44.1
013	75.0	−7.0	10750, 10750, 45	47	37.4	95	50.6
20791	46.0	−8.0	18800, 12400, 55	47	45.1	91	60.4
002	67.0	12.0	11900, 11900, 45	65	38.8	106	48.3
811	86.0	−13.0	9530, 9150, 0	54	43.2	101	59.2
96041	45.0	15.0	10800, 12000, 45	48	44.8	101	63.3
41117	141.6	−17.0	11000, 10500, 20	48	34.3	92	51.2
9571	87.0	−19.0	7150, 7150, 45	39	31.0	95	61.0
650	99.0	−19.0	8950, 8950, 0	42	43.4	94	57.4
9572	163.0	−19.0	7500, 7500, 45	39	37.0	95	60.6
9581	179.0	−20.0	6560, 6560, 0	51	36.8	105	54.0
004	11.0	−22.0	17500, 22500, 0	33	51.4	83	61.5
501	73.0	−30.0	9050, 10280, 0	36	44.1	53	56.3

Summary of the final TAXA (angle from tiltaxis to a^*), TANGL (tiltangle), and defocus values. In addition the number of spots up to IQ 5 and 8, respectively, are shown for each image together with their corresponding overall phase residual (ΔΦ) obtained by comparison against all other images in the data set. Defocus (underfocus) values are given in the form "defocus 1, defocus 2, angle between the direction of defocus 1 and the x axis in the transform". An overall phase residual of 90° would be obtained for a set of random data.

RESULTS

Characterization of the specimen

A total of about 1500 micrographs of crystals with tilt angles between 6 and 30° were recorded to extend the projection data obtained previously (Schertler et al., 1993). Out of these micrographs only about 1 in 100 showed spots beyond 20 Å resolution in the optical diffraction pattern.

The negatively stained crystal shown in Fig. 1 *a* demonstrates that ordered patches of rhodopsin molecules occupied only a small area of the vesicle surface, preferentially along straight edges. To emphasize the greatly reduced contrast of frozen hydrated specimens a cryo-preserved crystal is shown in Fig. 1 *b* for comparison. Although the lattice could not (or not easily) be detected by eye in these cases, diffraction spots out to about 10 Å resolution were visible by optical diffraction of the very best pictures. The calculated power spectrum from the best tilted crystal is shown as an example (Fig. 1 *c*). The approximate size of this crystal (0.29 μm × 0.44 μm) emphasizes that structural analysis exclusively relied on images, because electron diffraction patterns could not be recorded from such small crystals.

Image processing

To show that useful data beyond 10 Å resolution could nevertheless be obtained from this and images similar to that in Fig. 1, some of the intermediate image processing results are presented (Fig. 2). The shape and location of the crystal within the digitized area were well defined in the cross-correlation map after the first cycle of image filtering and lattice unbending. However, the efficiency of the unbending was increased by including all newly obtained measurements of at least 2.6 times the background intensity (IQ 3 or better) in the calculation of the filtered image and reference area of the next processing cycle. Normally this resulted in a 2.5-fold increase in the number of good cross-correlation peaks (≥70% similarity to the reference area from the middle of the image) after three cycles of processing. The improved cross-correlation map (Fig. 2 *a*) was used to box off the crystalline area before extracting the amplitudes and phases from its transform (Fig. 2 *c*). The statistical analysis of the peaks found in the various resolution bands (Fig. 2 *b*) indicated a weak but significant signal beyond 10 Å resolution. This was not the case if the crystal was not boxed off, because the ≈1800 unit cells inside the box did not diffract strongly enough to overcome the noise produced by the remaining non-crystalline area. In conclusion, multiple rounds of lattice straightening with improved reference areas and boxing of the crystalline area typically doubled the number of spots with intensities of at least 2.6-fold (IQ 3) above the background noise level.

Additional factors other than the absolute size of the crystal also limited the resolution obtainable from this and similar images. This became obvious from the final Fourier transform (Fig. 2 *d*) of the unbent second crystalline layer (Fig. 1 *c*). Although the size of this independent crystal was equivalent to the size of lattice "RE081A", the overall amount of preservation of structural detail is much lower for lattice "RE081B" (Fig. 2 *d*). The difference in defocus of about 900 Å between the two layers indicated that the vesicle was not completely collapsed and hence the two lattices were thought to be separated by a thin layer of vitrified water. This might have caused a stronger 3D disordering (by crinkling)

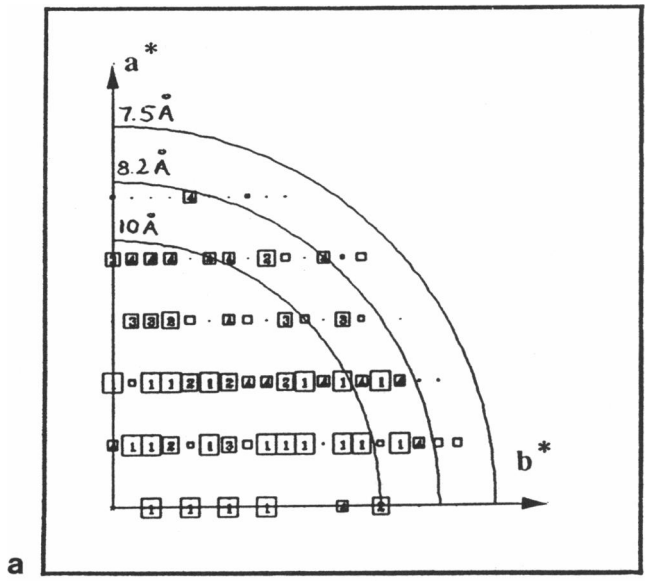

a

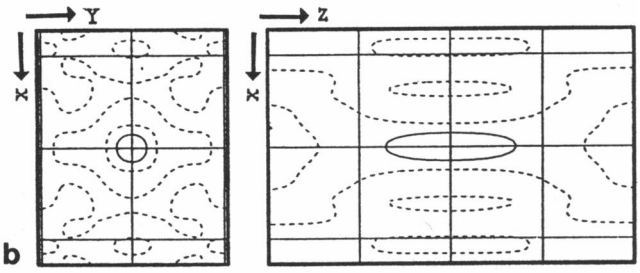

b

plane		half-width [Å]	effective resolution cut-off [Å]
x,y	x	6.0	9.4
	y	6.5	10.2
z,y	z	30.0	46.8
x,z	z	30.0	46.8

c

FIGURE 3 (*a*) Vectorially averaged phase errors for each individual reflection of the projection data. The numbers indicate a total error as follows: 1, ≤8°; 2, ≤14°; 3, ≤20°; 4, ≤25°; higher errors are indicated by decreasing box sizes. In this diagram a phase error of 90° is random. Circles represent resolutions of 10, 8.2, and 7.5 Å, respectively. (*b*) Sections through the point spread function of the experimental 3D data set, shown for the (*x*,*y*) and (*x*,*z*) planes. The impact of the low vertical resolution on the (*x*,*z*) plot can easily be seen. Solid contour lines represent the contour at half-height of the peak. The dotted lines are drawn at the zero contour level. The underlying grid lines have a spacing of 20 Å. (*c*) Summary of the effective resolution cutoffs obtained from the point spread function. The corresponding peak width for a simulated, ideal data set to 9 Å resolution and tilts up to 20° is 5.75 Å, i.e., a factor of 1.56 is obtained (9 Å/5.75 Å) for the conversion of the measured widths at half-height (half-widths) into effective resolution cutoffs.

of the layer, which was not in contact with the carbon film (i.e., lattice "RE081B" based on its smaller defocus), thereby reducing the resolution of data obtainable from this lattice.

TABLE 2 Image statistics

Resolution range in Å	Number of unique reflections	Mean ΔΦ
200–14	22	9.1°
14–10	26	20.8°
10–8.3	23	30.3°
8.3–7.5	15	46.1°

Number of images, 16; number of crystalline areas, 23; Total number of observations, 1314; total number of unique observations, 86; overall phase residual, 26.6° for all projection data to 7.5Å.

Image statistics of the projection data. Phase errors in the given resolution bands represent the mean of all individual reflections within a resolution band compared with their theoretical value based on the constraints of the point group. For point group $p222_1$ all phases are constrained to 0° or 180° in projection except for odd (0, *k*) reflections, which are absent because of the twofold screw axis along *b*. Due to the phase constraints, a mean phase error of 45° indicates random phases. All mean phase errors out to 8.3 Å are significantly better than those published previously (Schertler et al. 1993). This is due to the larger number of data included in the current dataset and reflects its increased reliability.

A more general lack of specimen flatness could also explain why the image amplitudes faded out more quickly in a direction perpendicular to the tilt axis for both crystals.

Merging of data and evaluation of the resolution of the final data set

After processing about 45 crystalline areas, the best 23 areas were selected for the merged data set. A summary of the details for each film is given in Table 1. All measurements with a signal-to-noise ratio of at least 1.6 (IQ 5 or better) were used to determine and refine the common phase origin for the individual transforms. The origins did not change significantly if the weaker data (up to IQ 8) were included, and hence all data were used to fit lattice lines. Only unambiguously defined parts of the transform were included in the final list of structure factors. Analysis of the image statistics for the projection data (Fig. 3 *a* and Table 2) indicated that the

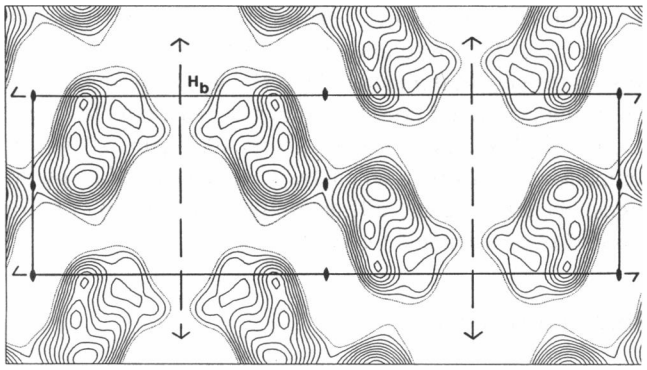

FIGURE 4 Projection density map of bovine rhodopsin calculated from the 3D data set. In this figure the image amplitudes were not treated for the resolution-dependent loss of intensity. Shown is the equivalent of one-unit cell with cell dimensions a = 43 Å, b = 140 Å, and γ = 90°. The twofold axes along a and c as well as the twofold screw axis along b are indicated in the map. The label H_b refers to a structural feature discussed in more detail in context with the 3D maps (see Figs. 5 and 8).

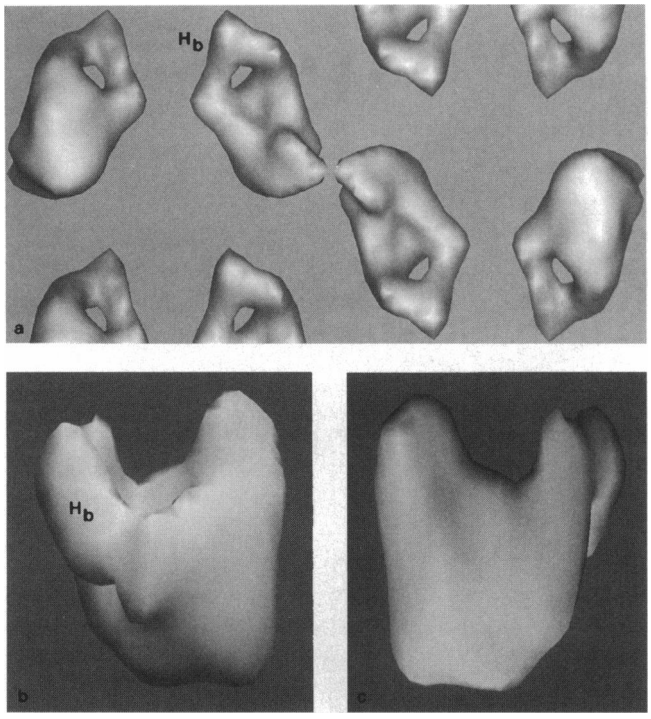

FIGURE 5 (*a*) Surface representation of the unsharpened 3D map of bovine rhodopsin seen downward along the *c* axis. The different appearance of the extracellular and intracellular sides of rhodopsin allows the twofold screw axis along *b* to be seen very clearly. The marked part (H_b) of the rhodopsin molecule to the left of the central twofold axis corresponds to the sloping surface region described in the text and also correlates this part of the molecule with the equivalent part in the side view shown in *b*. (*b*) Side view of a single unsharpened rhodopsin molecule. The marked density feature H_b corresponds to the sloping surface region mentioned in the text. The upper left end of H_b faces the observer in the molecule marked in *a*. (*c*) Side view of an unsharpened rhodopsin molecule looking from the opposite direction to that in *b*.

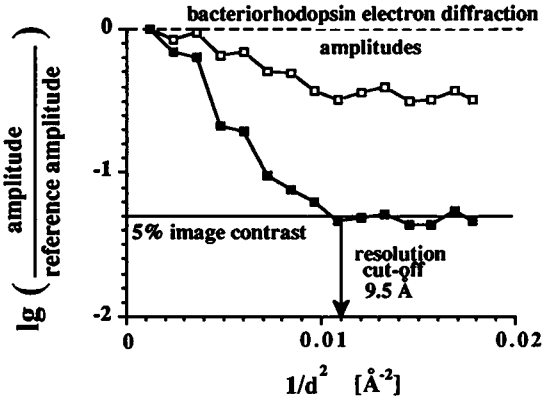

FIGURE 6 Comparison of the resolution-dependent fadeout of the image amplitudes observed for bacteriorhodopsin (□) and rhodopsin (■) projection data. Electron diffraction data of untilted bacteriorhodopsin crystals were used as reference to determine the fall-off of the image amplitudes with increasing resolution. The level where the rhodopsin image amplitudes are reduced to 5% of the image contrast found at resolutions below 30 Å (i.e., ≤ 0.001 Å^{-2}) is marked by a solid line. At this point the observed fadeout starts to deviate from a straight line, indicating that the amplitudes have reached the level of the background noise. The corresponding resolution of 9.5 Å represents the cutoff to which data were scaled. The scale factor (B) relating the resolution cutoff (d) to the residual image contrast is defined by $\ln(\text{image contrast}) = -B/4d^2$. In this case a temperature factor of $B = -1000$ Å^2 was obtained.

resolution within the membrane plane is about 9 Å. This cutoff was apparent in the phase errors calculated for each reflection (Fig. 3 *a*) and the agreement of the measured phases compared with their theoretical values based on symmetry constraints of the point group (Table 2). In addition, the point spread function was calculated to evaluate more objectively the resolution of the whole 3D data set (Fig. 3 *b* and *c*). Compared with an ideal dataset of 9 Å horizontal resolution and tilt angles up to 20°, the real data were only 62.5% complete. Their calculated resolution cutoffs within the plane were 9.4 and 10.2 Å in *x* and *y*, respectively. This result agreed with the alternative estimates obtained for the projection data. The vertical resolution cutoff obtained from the point spread function was about 47 Å. Given that this resolution indicates that any 3D map will be substantially blurred in the *z* direction, the approximate position of only those α-helices that are almost perpendicular to the plane of the membrane could be expected to be seen.

The low resolution structure of bovine rhodopsin

A projection density map of rhodopsin (Fig. 4) at a nominal resolution of 9 Å lacked high resolution details because the map was dominated by the strong low resolution structure factor amplitudes out to about 16 Å. Nevertheless, the general organization and the $p222_1$ symmetry of the rhodopsin molecules within the crystal lattice could easily be detected. In addition, it became obvious that the crystal is formed by only a small number of protein-protein contacts. This could be seen even better in a surface representation of a 3D map calculated to the same resolution limit (Fig. 5 *a*). This display

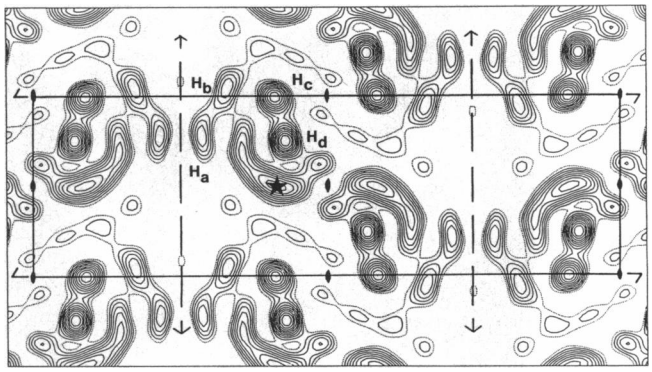

FIGURE 7 Sharpened projection density map of bovine rhodopsin at 9 Å resolution. The symmetry operators relating the four molecules within the unit cell are shown as in Fig. 4. A temperature factor of $B = -1000$ Å^2, obtained from Fig. 6, was applied to rescale the image amplitudes. The four clearly resolved peaks marked H_a, H_b, H_c, and H_d can be interpreted to arise from transmembrane helices oriented almost perpendicular to the plane of the membrane, taking into account the overall size of rhodopsin and the fact that about 50% of all its residues reside within the membrane. In contrast, the unresolved "arc-shaped" density marked by the asterisk most likely reflects the overlapping signals of three more highly tilted helices.

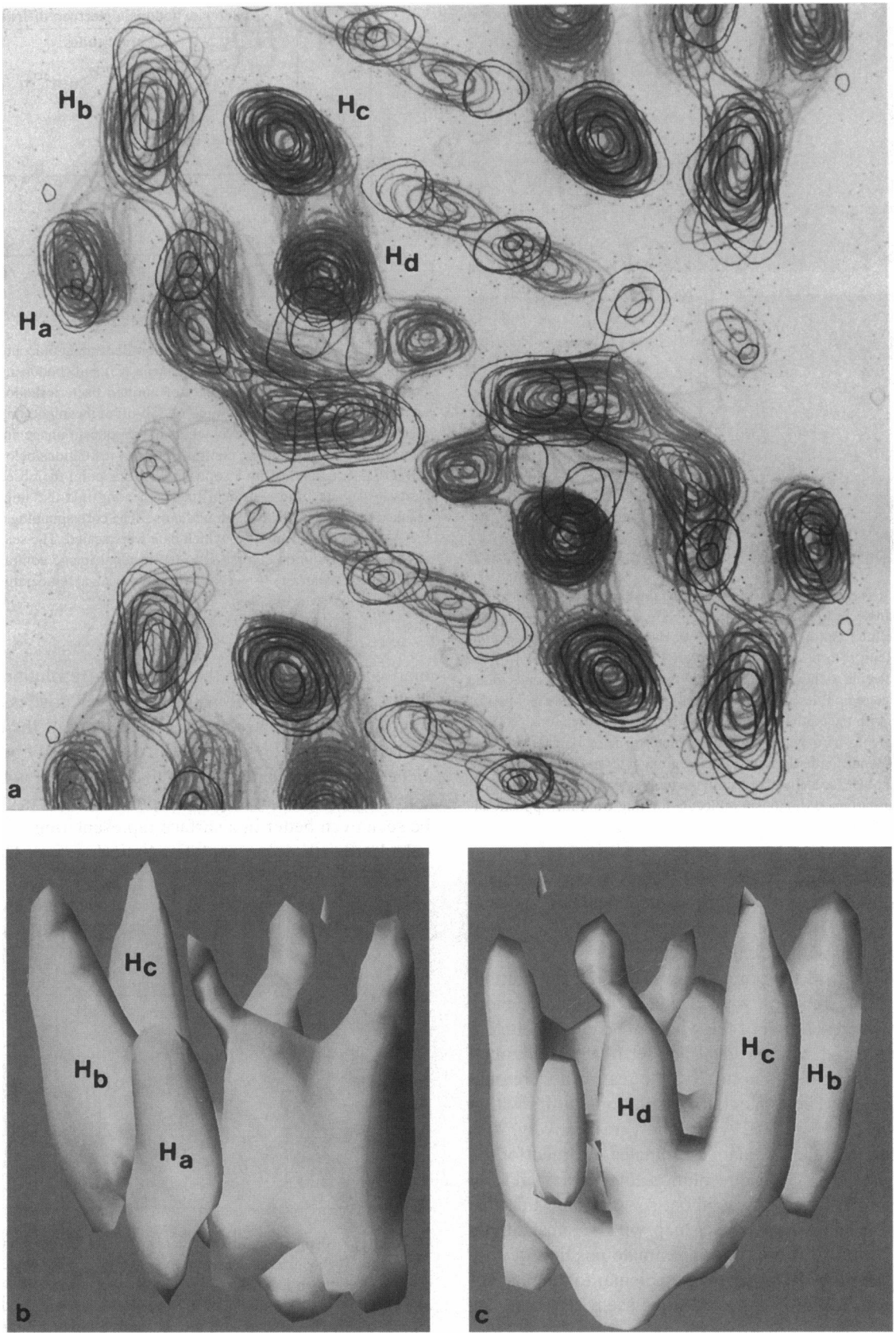

FIGURE 8 (*a*) Stack of contour plots of the sharpened 3D map of bovine rhodopsin seen downward along the direction of *c* (*top view*). Only the pair of molecules around the central twofold axis is fully shown. For the left molecule the four clearly resolved features H_a, H_b, H_c, and H_d are marked. These labels are referred to in the text and they are used to correlate the top view with the two side views (*b* and *c*). They also refer back to Figs. 7, 4 (H_b only), and 5 (H_b only). It should be stressed that the labels are only used for the purpose of discussion. They are not meant to represent assignments of the helices

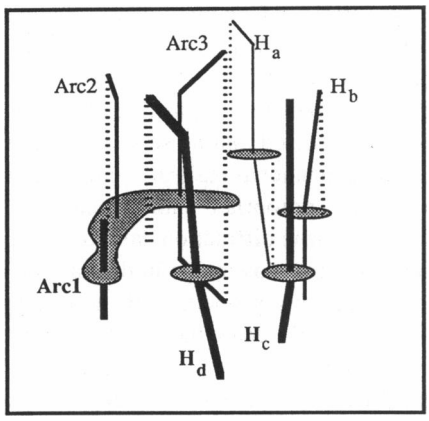

FIGURE 9 Schematic representation of the tracks of densities observed in the sharpened 3D map (Fig. 8 *a*) of bovine rhodopsin, seen from the direction of view presented in Fig. 8*c*. Shaded areas represent a simplified view of features seen in the projection structure. Solid lines indicate the positions of the centers of densities observed in the "arc-shaped" region (Arc1, Arc2, and Arc3) and the resolved densities H_a, H_b, H_c, and H_d if followed through the contoured sections. The very bottom sections of the map were excluded in this drawing, because the peaks found there could not be unambiguously assigned to one of the density features mentioned. Dotted lines indicate onto which part of the molecule the end of the respective density track would be projected. The drawing is not to scale.

also emphasized that the extracellular and intracellular surface of rhodopsin are quite different. A single rhodopsin molecule appeared as a particle with planar dimensions of 42 Å × 20 Å on one side of the membrane and 31 Å × 22 Å on the opposite side. One of the most striking features was a sloping surface region (marked H_b in Fig. 5 *b*), which corresponded to one of the four clearly resolved peaks in the projection structure published previously (Schertler et al., 1993). This suggested that the helix, which this density represents, is more tilted than anticipated from the projection map.

To make full use of the phase information obtained from the images (Fig. 3 *a*) and to obtain a more detailed map representing the true resolution contained in the data, the image amplitudes were corrected for the resolution-dependent loss of contrast (Havelka et al., in press; Henderson, 1992). The projection data were used to obtain a measure for the amount of amplitude weighting necessary to restore the full amount of information. A comparison of image amplitudes for rhodopsin and bacteriorhodopsin with electron diffraction data obtained for untilted 2D crystals of bacteriorhodopsin (Fig. 6) showed that the resolution-dependent loss in intensity was much more pronounced in the case of bovine rhodopsin. This was thought to be caused by the much higher degree of disorder in the rhodopsin crystals, because it is known that the fadeout observed for the image amplitudes obtained from very well-ordered bacteriorhodopsin crystals is primarily caused by imaging defects (Henderson, 1992). More importantly, the comparison shown in Fig. 6 allowed the determination of an appropriate scaling factor for the rhodopsin image amplitudes. The deviation of the fall-off from an almost straight line at about 9.5 Å resolution and a residual image contrast of about 5% specified the point where the image amplitudes began to level out at the magnitude of the random background noise. The required scale factor of $B = -1000$ Å^2 was calculated from these figures according to

$$\ln(\text{image contrast}) = -B/4d^2 \qquad (1)$$

where B represented a general temperature factor and d the resolution to which data could be scaled. Consequently, the intensities for reflections at 9 Å resolution were scaled up about 22-fold to restore their appropriate weight. To be able to do this, the input data had to be well defined, because this procedure scaled up the noise as well as the real data.

The effect of this scaling procedure is shown in Fig. 7, for which the same set of data was used as for the generation of Fig. 4. In contrast to the projection density map obtained without scaling of the amplitudes (Fig. 4), the sharpened map (Fig. 7) displayed several distinct features that were similar to those displayed in the map derived from untilted images (Schertler et al., 1993). A direct comparison of the two projection density maps (Figs. 4 and 7) showed that some of the densities observed in the map were unlikely to be part of the polypeptide. These additional peaks presumably represented a combination of noise amplified by the sharpening procedure and the absence of those projection structure factors for which no phases could be assigned.

The scaling of the whole data set allowed a sharpened 3D map to be calculated. Seen downward along the *c* axis (Fig. 8 *a*), it became apparent how the different parts of the molecule add up to produce the projected structure. The temperature factor used for scaling was the same as for the projection data ($B = -1000$ Å^2). As for the unsharpened map, surface representations of two different views of a single rhodopsin molecule are given (Fig. 8, *b* and *c*). Based on the

to any specific hydrophobic segments in the rhodopsin sequence. (*b*) Surface representation of a single sharpened rhodopsin molecule as seen from the side. The direction of view is the same as in Fig. 5 *b*, and some density features are marked to correlate the view with the top view given in Fig. 8 *a*. Part of the unresolved "arc-shaped" density feature can be seen to the right with some sloping features protruding from its main body of density. In contrast H_a, H_b, and H_c form three distinct density features. These rods of density most likely represent transmembrane helices. From this diagram it is clear that they are only slightly or not all all tilted with respect to the plane of the membrane. However, if compared directly, it appears that feature H_b is slightly more tilted than the other three resolved tracks of density. Interestingly, all three features can already be detected in the equivalent side view of the unsharpened map (Fig. 5 *b*). (*c*) View from the opposite direction to that shown in *b*. The three resolved features H_b, H_c, and H_d and the remaining part of the "arc-shaped" feature can clearly be seen. The apparent "v shape" formed by H_c and H_d can be explained best by the presence of an extramembranous part of the polypeptide at the bottom side of the molecule. In this case one would expect its density to merge with some of the density of the helices due to the stretching out of mass caused by the low vertical resolution. For the same reason, the merging of H_d with the unresolved "arc" even farther down and across the bottom of the molecule is most certainly caused by parts of the polypeptide that do not reside within the membrane. For reasons discussed in more detail in the text, the short and straight density feature to the left of H_d does not represent a resolved helix but belongs to the unresolved "arc-shaped" density.

top view (Fig. 8 *a*), the short, apparently straight stretch of density found to the left of H_d in Fig. 8 *c* (see also "Arc1" in Fig. 9) was thought to be a part of the unresolved, "arc-shaped" region and will be discussed later. In contrast, the well-defined peaks marked H_a, H_b, H_c, and H_d in Fig. 7 corresponded to four rods of density (Fig. 8, *b* and *c*) and were interpreted as four α-helices oriented almost perpendicular to the plane of the membrane. However, Fig. 8, *a* and *b* also show that H_b appeared to be more tilted than H_a, H_c, and H_d. In addition, its slope agreed well with the sloping surface region observed in the unsharpened map (Fig. 5 *b*).

DISCUSSION

2D crystals of bovine rhodopsin have been generated by reconstitution into phosphatidylcholine bilayers (Schertler et al., 1993). Here we present a low resolution 3D map based on electron cryo-microscopy of tilted 2D crystals in vitrified water. The small size and disorder of the crystals precluded electron diffraction, and the analysis was based entirely on image data. Maps with the greatest detail were obtained by two improvements in image processing, 1) multiple cycles of lattice straightening and 2) scaling of image amplitudes to correct for the resolution-dependent loss of intensity. The much more pronounced degradation of the image amplitudes as opposed to direct electron diffraction amplitudes obtained from disordered crystals is a known, yet poorly understood limiting effect in structure reconstructions from high resolution electron micrographs (Henderson, 1992; Henderson and Glaeser, 1985) and must be taken into account. It also explains why the combination of electron diffraction amplitudes with phases obtained from images is the preferred approach for the determination of protein structures by high resolution electron microscopy. However, the resolution-dependent fadeout of the image amplitudes can be corrected for within certain limits. A comparison of Figs. 5 and 8 shows the effect of such an amplitude scaling procedure very clearly. It also emphasizes that the sharpening mainly enhances the appearance of features that can already just be detected in the unsharpened map. However, the amplitude scaling cannot compensate for the intrinsic low vertical resolution of the data. Despite the positive effect of the sharpening it has to be stressed that noise in the data will be amplified in the same manner as real data, and therefore care has to be taken to apply appropriate scaling factors. In this sense, the existence of electron diffraction data for bacteriorhodopsin represents a distinct advantage in the case of rhodopsin, as the general scattering properties of the two proteins are thought to be similar. Based on their molecular weights, rhodopsin is expected to scatter only about 1.3-fold more strongly than bacteriorhodopsin. Furthermore, it seems reasonable to assume that as with bacteriorhodopsin the bundle of transmembrane helices is the strongest scattering feature in rhodopsin, and hence the overall radial distribution of electron diffraction amplitudes from bacteriorhodopsin provides a direct guideline for how the rhodopsin image amplitudes should be corrected for their resolution-dependent loss of image contrast. Anisotropic scaling of the 3D data contained in each image before lattice line fitting (Havelka et al., in press), using either bacteriorhodopsin or electron form factors as a reference, did not change the appearance of the map significantly. This is most likely due to the limited amount of vertical resolution data in the individual images and emphasized again that the isotropic scaling used to generate the sharpened maps primarily affects and enhances the horizontal resolution of the data.

Although the planar resolution is 9 Å and the vertical resolution is only 47 Å, four of the seven transmembrane-spanning α-helices can be resolved. It should be noted that these four helices are real features and do not reflect series termination errors due to the truncation of the transform at 9 Å. The strongest argument to support this view comes from 6 Å projection structures of frog rhodopsin obtained for two independent crystal forms (Schertler and Hargrave, submitted for publication). These projections are compatible with the findings in our study even to the point that helix H_b is more highly tilted than previously anticipated.

The remaining three transmembrane helices of rhodopsin are not yet resolved to the same extent. This fact comprises the strongest experimental proof to date that these three helices must be more highly tilted, as the data obtained from tilts up to 20° are not enough to resolve sufficient details in the "arc-shaped" feature to be able to correlate directly the observed density distribution with individual α-helical transmembrane segments. This becomes obvious especially if the three distinct centers of density, which are observed in this region, are traced throughout the map (Fig. 8 *a*). A schematic representation of the result is presented in Fig. 9 where Arc1, Arc2, and Arc3 represent the traces of the centers of mass for these three distinct density features. Taking into account the poor vertical resolution, the displacements of density at the top and bottom of Arc2 and Arc3 off their vertical main axes are too big to represent resolved features. They are, however, compatible with the overlapping signals of tilted helices that have not been resolved. An additional clue supporting this

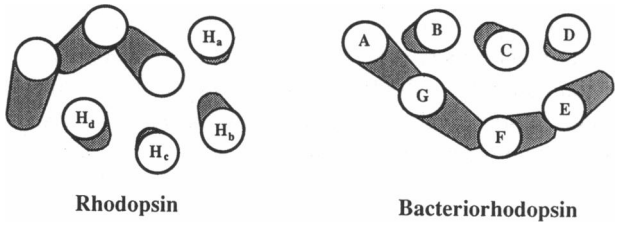

FIGURE 10 Adaptation of the model of rhodopsin proposed by Baldwin (1993) and comparison with bacteriorhodopsin. Both molecules are shown in equivalent orientations. The four resolved helices in rhodopsin have been marked to correlate the model with the experimental map (Fig. 8). The remaining three helices were not marked, because they do not correspond to the observed features Arc1, Arc2, and Arc3 outlined in Fig. 9. However, the discussion of Fig. 9 in the text makes it clear how these features relate to the three unmarked helices. The assignment of the helices in bacteriorhodopsin is known and the particular view shown in Fig. 10 represents bacteriorhodopsin as seen from the intracellular side. It becomes clear that the detailed arrangement of the helices in the two molecules is not the same.

view can be obtained from the density feature Arc1. Because of the low vertical resolution all densities in the map are stretched out by about 30 Å, i.e., the half-width of the point spread peak along z. This vertical blurring of density causes the real length of any of the putative helices to be overestimated and once more emphasizes that only the helices oriented almost normal to the plane of the membrane are being resolved. Accordingly, density feature Arc1 (Fig. 9) cannot represent a resolved helix in its own right, as it only extends over about 30 Å in the map (Fig. 8 *a*). Because this is an overestimate of its real length (for the reason mentioned above), some additional density is needed to allow for a complete transmembrane segment. Most likely, this additional density is represented by the displaced density at the top of feature Arc2. Similar discontinuities in density traces of tilted helices have been observed in the early stages of the structure determination of bacteriorhodopsin (R. Henderson, personal communication). In this interpretation the true helix at this position in the rhodopsin structure would be sloping away from the observer if looked at as shown in Fig. 9, i.e., from the bottom of density feature Arc1 toward the top of density feature Arc2. As a direct consequence one would expect the remaining two helices in the "arc" to be tilted in the same general direction, because otherwise no meaningful packing of the helices can be achieved. However, it must be stressed that, despite this interpretation providing the best explanation for the observed density distribution within the "arc", it is solely based on a number of weak indications in the map.

An assignment of the four clearly resolved helices to individual hydrophobic stretches in the rhodopsin sequence is not possible based on the data presented here. However, their position in the map agrees with the tentative model suggested by Baldwin (1993). Baldwin's structural constraints for each of the transmembrane helices in rhodopsin were based on an analysis of 205 G protein-coupled receptor sequences. These constraints enabled Baldwin (1993) to assign the peaks observed in the published projection structure (Schertler et al., 1993) to individual transmembrane helices in the rhodopsin sequence and allowed her to extend the projection structure into a tentative 3D model of rhodopsin. An adaptation of the model proposed by Baldwin (1993) to our experimental data is shown in Fig. 10, which also includes an equivalent drawing for bacteriorhodopsin. The comparison of the rhodopsin 3D structure with bacteriorhodopsin shows that the arrangement of the individual helices is significantly different, despite a similar overall membrane topology.

CONCLUSION

Electron cryo-microscopy of small 2D crystals of bovine rhodopsin and image reconstruction has allowed the calculation of a 3D structure of a G protein-coupled receptor. Scaling of the image amplitudes to compensate for the resolution-dependent loss of contrast revealed details just beyond 10 Å resolution within the plane of the membrane. Four of the seven α-helices were clearly resolved. This confirmed the interpretation of the projection structure of rhodopsin published previously (Schertler et al., 1993). However, one of the four helices that looked almost perpendicular to the plane of the membrane appears to be more tilted in the 3D map. This result is also supported by 6 Å projection structures of frog rhodopsin, obtained from two independent crystal forms (G. F. X. Schertler and P. A. Hargrave, submitted for publication). The experimental data obtained by us have been compared to the tentative model of rhodopsin suggested by Baldwin (1993). The four clearly resolved helices agree well with this model, which also provides the best interpretation for the density distribution in the yet-unresolved "arc-shaped" part of the structure. Accordingly, it seems very likely that the transmembrane part of the rhodopsin structure consists of a group of four tilted helices forming an extended "arc", which is flanked by an untilted helix (H_a in Fig. 8) on the outer side of the "arc" and a pair of straight helices (H_c and H_d in Fig. 8) on its inner side. This arrangement of helices clearly shows that, despite their similar membrane topology, the detailed structures of rhodopsin and bacteriorhodopsin are significantly different.

We would like to thank C. Villa for technical support in preparing rhodopsin and obtaining the crystals, J. Baldwin for help with the calculation of the point spread function, and R. Beroukhim for help with the AVS package. We would also like to thank the referees for their helpful comments on the first version of the manuscript. Finally, we would like to thank R. Henderson for continuous support and advice during the data collection and image processing.

REFERENCES

Agard, D. A. 1983. A least-squares method for determining structure factors in three-dimensional tilted-view reconstructions. *J. Mol. Biol.* 167:849–852.

Baldwin, J. M. 1993. The probable arrangement of the helices in G protein-coupled receptors. *EMBO J.* 12:1693–1703.

Baldwin, J. M., R. Henderson, E. Beckman, and F. Zemlin. 1988. Images of purple membrane at 2.8 Å resolution obtained by cryo-electron microscopy. *J. Mol. Biol.* 202:585–591.

Chabre, M. 1978. Diamagnetic anisotropy and orientation of α-helix in frog rhodopsin and meta II intermediate. *Proc. Natl. Acad. Sci. USA.* 75:5471–5474.

DeGrip, W. J. 1982. Purification of bovine rhodopsin over Concanavalin A-sepharose. *Methods Enzymol.* 81:197–207.

Fresenko, E. E., S. S. Kolesnikov, and A. L. Lyubarsky. 1985. Induction by cyclic GMP of cationic conductance in plasma membrane of retinal rod outer segment. *Nature.* 313:310–313.

Hargrave, P. A., J. H. McDowell, D. R. Curtis, J. K. Wang, E. Juszczak, S. L. Fong, J. K. M. Rao, and D. P. Smith. 1983. The structure of bovine rhodopsin. *Biophys. Struct. Mech.* 9:235–244.

Havelka, W. A., R. Henderson, and D. Oesterhelt. Three-dimensional structure of Halorhodopsin at 7Å resolution. *J. Mol. Biol.* In press.

Henderson, R. 1992. Image contrast in high-resolution electron microscopy of biological macromolecules: TMV in ice. *Ultramicroscopy.* 46:1–18.

Henderson, R., J. M. Baldwin, T. A. Ceska, F. Zemlin, E. Beckmann, and K. H. Downing. 1990. Model for the structure of bacteriorhodopsin based on high-resolution electron cryo-microscopy. *J. Mol. Biol.* 213:899–929.

Henderson, R., J. M. Baldwin, K. H. Downing, J. Lepault, and F. Zemlin. 1986. Structure of purple membrane from *Halobacterium halobium*: recording, measurement and evaluation of electron micrographs at 3.5 Å resolution. *Ultramicroscopy.* 19:147–178.

Henderson, R., and R. M. Glaeser. 1985. Quantitative analysis of image contrast in electron micrographs of beam-sensitive crystals. *Ultramicroscopy.* 16:139–150.

Kühlbrandt, W., D. N. Wang, and Y. Fujiyoshi. 1994. Atomic model of plant light-harvesting complex by electron crystallography. *Nature*. 367:614–621.

Lamba, O. P., D. Borchman, and P. J. O'Brien. 1994. Fourier transform infrared study of the rod outer segment disk and plasma membranes of vertebrate retina. *Biochemistry*. 33:1704–1712.

Michel-Villaz, M., H. Saibil, and M. Chabre. 1979. Orientation of rhodopsin α-helices in retinal rod outer segment membranes studied by infrared linear dichroism. *Proc. Natl. Acad. Sci. USA*. 76:4405–4408.

Ovchinnikov, Y. A., N. G. Abdulaev, M. Y. Feigina, I. D. Artamonov, A. S. Zolotarev, M. B. Kostina, A. S. Bogachuk, A. I. Miroshnkov, V. I. Martinov, and A. B. Kudelin. 1982. The complete amino acid sequence of visual rhodopsin. *Bioorg. Khim.* 8:1011–1014.

Saibil, H., M. Chabre, and D. Worcester. 1976. Neutron diffraction studies of retinal rod outer segment membranes. *Nature*. 262:266–270.

Sakmar, T. P., R. R. Franke, and H. G. Khorana. 1989. Glutamic acid-113 serves as the retinylidene Schiff base counterion in bovine rhodopsin. *Proc. Natl. Acad. Sci. USA*. 86:8309–8313.

Schertler, G. F. X ., C. Villa, and R. Henderson. 1993. Projection structure of rhodopsin. *Nature*. 362:770–772.

Shichi, H., and J. Shelton. 1974. Assessment of physiological integrity of sonicated retinal rod membranes. *J. Supramol. Struct.* 2:7–16.

Toyoshima, C., H. Sasabe, and D. L. Stokes. 1993. Three-dimensional cryo-electron microscopy of the calcium ion pump in the sarcoplasmic reticulum membrane. *Nature*. 362:469–471.

Unwin, N. 1995. Acetylcholine receptor channel imaged in the open state. *Nature*. 373:37–43.

Unwin, P. N. T. 1993. Nicotinic acetylcholine receptor at 9 Å resolution. *J. Mol. Biol.* 229:1101–1124.

Unwin, P. N. T., and R. Henderson. 1975. Molecular structure determination by electron microscopy of unstained crystalline specimens. *J. Mol. Biol.* 94:425–440.

Zhukovsky, E. A., and D. D. Oprian. 1989. Effect of carboxyclic acid side chains on the absorption maximum of visual pigments. *Science*. 246: 928–930.